FABRICATION, TREATMENT, AND TESTING
OF MATERIALS AND STRUCTURES

Structure, Composition, and Properties of Zn- and O-Ion Implanted Silicon at Elevated Temperatures

V. V. Privezentsev[a,b,*], A. P. Sergeev[a], V. S. Kulikauskas[c], D. A. Kiselev[d],
A. Yu. Trifonov[e,f], and A. N. Tereshchenko[g]

[a] *FRC Scientific Research Institute of System Analysis, Russian Academy of Sciences, Moscow, 117218 Russia*
[b] *Valiev Institute of Physics and Technology, Russian Academy of Sciences, Moscow, 117218 Russia*
[c] *Skobeltsyn Institute of Nuclear Physics, Moscow State University, Moscow, 119991 Russia*
[d] *National University of Science and Technology "MISiS", Moscow, 119049 Russia*
[e] *National Research University "MIET", Moscow, Zelenograd, 124432 Russia*
[f] *Lukin Scientific Research Institute of Physical Problems, Moscow, Zelenograd, 124432 Russia*
[g] *Institute of Solid-State Physics, Russian Academy of Sciences, Chernogolovka, Moscow oblast, 142432 Russia*
*e-mail: v.privezentsev@mail.ru
Received August 5, 2020; revised August 15, 2020; accepted August 15, 2020

Abstract—Czochralski-grown Si substrates (*n*-type, orientation (100)) are subjected to double implantation, notably, initially by $^{64}Zn^+$ ions with a dose of 5×10^{16} cm^{-2} and an energy of 50 keV and then with $^{16}O^+$ ions with a dose of 2×10^{17} cm^{-2} and an energy of 20 keV. The substrates during implantation are held at ~350°C. The implanted Si substrates contain radiation-induced defects and their clusters such as twins, dislocations, and nanoclusters, notably, Zn-containing nanoclusters with an average radius of 10–50 nm predominantly consisting of the metallic Zn phase and partially from the ZnO phase formed on the surface and in the substrate near-surface layer. Photonic annealing to an effective temperature of 700°C optimal for the formation of the ZnO phase leads to the annealing of radiation-induced defects, and Zn-containing nanoclusters presumably consisting of the ZnO phase and partially of the Zn_2SiO_4 phase with an average diameter of 50–100 nm are recorded on the sample surface.

1. INTRODUCTION

The properties of metallic and metal-oxide nanoparticles (NPs) in semiconducting and transparent dielectric matrices are widely studied because of the prospects of their application in modern optoelectronic and microelectronic devices [1]. Zinc-oxide NPs play an important role because ZnO is a direct-gap material with a band gap of 3.37 eV and has a large exiton binding energy of 60 meV. Therefore, zinc-oxide NPs can be used in light-emitting devices of the ultraviolet range [3, 4]. Due to other unique properties of ZnO such as the sorption effect, piezoelectricity, and ferromagnetism even at room temperature, they can be applied in solar cells [5], gas sensors [6], spintronic devices [7], memory devices (memristors) [8], in medicine [9], and biology [10].

Since Si has been preferentially used in microelectronics up to now, the presence of zinc and ZnO NPs in a Si substrate causes special interest. The formation of such NPs with controlled sizes and shape is of considerable practical significance. There have been several attempts to form Zn and ZnO nanoparticles in Si by the implantation of Zn and subsequent thermal oxidation of the implanted silicon plates [11–13]. We previously reported our investigations into the formation of Zn and ZnO nanoparticles in Si substrates implanted by Zn ions at elevated temperatures with subsequent annealing in an oxygen atmosphere [14]. In this work, we present the results of studying NP formation in Si substrates sequentially implanted with Zn and O at elevated temperatures.

2. EXPERIMENTAL

Czochralski-grown *n*-type Si substrates with the orientation (100) were implanted initially with $^{64}Zn^+$ ions with the dose 5×10^{16} cm^{-2} and an energy of 50 keV and then by $^{16}O^+$ ions with the dose 2×10^{17} cm^{-2} and an energy of 20 keV. The substrate temperature at both implantation stages was ~350°C. Then the substrates were cut into samples 10×10 mm in size, and these samples were subjected to isochronic (for 20 min) photonic annealing in vacuum. The
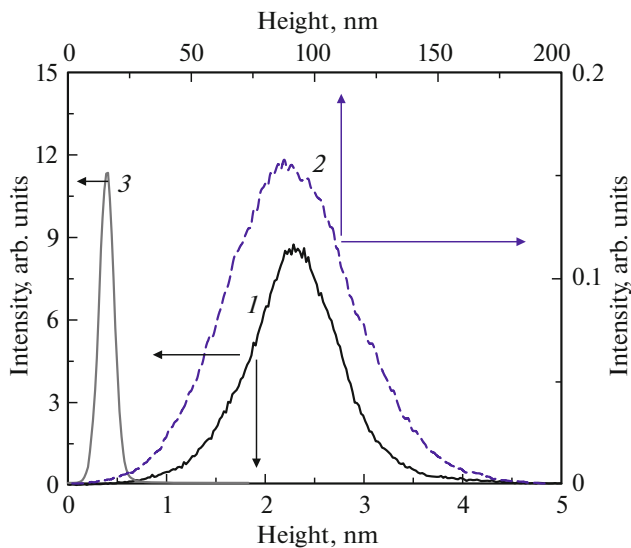
Fig. 1. Roughness histograms for the samples under study: *1*—Si sample after Zn/O implantation, *2*—Si sample after photonic annealing at an effective temperature of 700°C, and *3*—silicon substrate with a natural SiO$_2$ layer.

effective temperature at each photonic annealing stage was from 500°C to 900°C with a step of 100°C.

The sample topography was studied using a scanning probe microscope MFP-3D (Asylum Research) in the tapping atomic-force mode (AC Air Topography) and in the Kelvin mode. The profiles of the implanted impurities Zn and O as well as of accompanying oxide ions, which were formed in the implanted sample during annealing, were studied by secondary-ion mass spectrometry using a time-of-flight ToF.SIMS 5−100 mass spectrometer (ION-TOF). The samples were sputtered during layer-by-layer analysis by O$_2^+$ ions with an energy of 0−5 keV when analyzing the positive secondary ions of Si, O, and Zn; and by Cs$^+$ ions with an energy of 0.5 keV when analyzing the negative secondary ions of O, Si, SiO, SiO$_2$, ZnO, and Zn$_2$SiO$_4$. The energy of the analyzing Bi$^+$ beam was 30 keV. Photoluminescence (PL) measurements were performed at a temperature of 10 K according to the standard phase-sensitive procedure with a cooled germanium photoresistor used as the detector. PL was excited by photons with a wavelength of $\lambda = 920$ nm with an excitation density of 10 mW/mm^2.

3. RESULTS AND DISCUSSION

3.1. Scanning Probe Microscopy

The surface of the initial Si substrate is rather smooth and its roughness is smaller than 0.1 nm, while the roughness-distribution maximum is ~0.5 nm (Fig. 1, curve *3*). Figure 2a shows a 2D atomic force

microscopy (AFM) image, and Fig. 2b shows a 3D AFM image of the surface of the Si-substrate samples after hot Zn/O implantation. Figure 1 shows the roughness distribution over the entire square frame for this case (curve *1*). It follows from the analysis of Fig. 2 that the sample surface after hot Zn/O implantation becomes more inhomogeneous when compared with the initial state before implantation. The roughness parameters are now as follows: Rms = 0.58 nm, Ra = 0.43 nm, and the roughness maximum is 2.3 nm (Fig. 1, curve *1*). The surface consists of hillocks and valleys. The hillocks are round in shape with an in-plane size in the range of 20−50 nm. These rounded hillocks are surrounded by valleys with approximately the same in-plane size (Fig. 2). The observed hillocks are caused by Zn-containing nanoclusters (predominantly Zn and/or ZnO) and radiation-induced defects (see further the TEM section), which are formed after implantation.

Figure 3a shows the 2D AFM image of the sample surface after pulsed light annealing in vacuum at an effective temperature of 700°C. The roughness distribution over the entire frame for this case is presented in Fig. 1 (curve *2*). The roughness parameters for this case are as follows: Rms = 26 nm, Ra = 21 nm. It is seen that the sample surface after annealing becomes more structured (Fig. 3b), notably, its roughness increases considerably, so that its average values reach 90 nm (Fig. 2, curve *2*). The surface consists of hillocks and valleys. Both types of these surface asperities have in-plane sizes of ~100 nm. The formed hillocks are caused by Zn-containing nanoclusters, mainly consisting of the ZnO phase and/or the Zn$_2$SiO$_4$ phase, which are formed after photonic annealing.

3.2. Time-of-Flight Secondary-Ion Mass Spectrometry

Figure 4 shows the distribution profiles over the sample depth for Zn (curve *2*) and O (curve *1*) immediately after implantation as well as after annealing (curve *4* for Zn and curve *3* for O). Calibration of the profiles of Zn$^+$ and O$^-$ in the sample after implantation (curve *2*) was performed according to the known implantation doses. The maximal Zn concentration of 8.6×10^{21} cm^{-3} is found at a depth of 50 nm. The distribution of implanted Zn, in addition to the main maximum that was discussed above, has an additional surface maximum at a depth of ~5 nm of approximately same magnitude. The latter can be associated with zinc segregation due to the presence of a surface layer of silicon oxide.

As for the profile of implanted oxygen after Zn/O implantation, the maximal O$^-$ concentration of $1-2 \times 10^{22}$ cm^{-3} is found at a depth of 55 nm. However, the distribution of O$^-$, in addition to the main maximum that was discussed above, has an additional surface maximum at a depth of ~5 nm with a value of 4.5×10^{22} cm^{-3}. This can be associated with the presence of
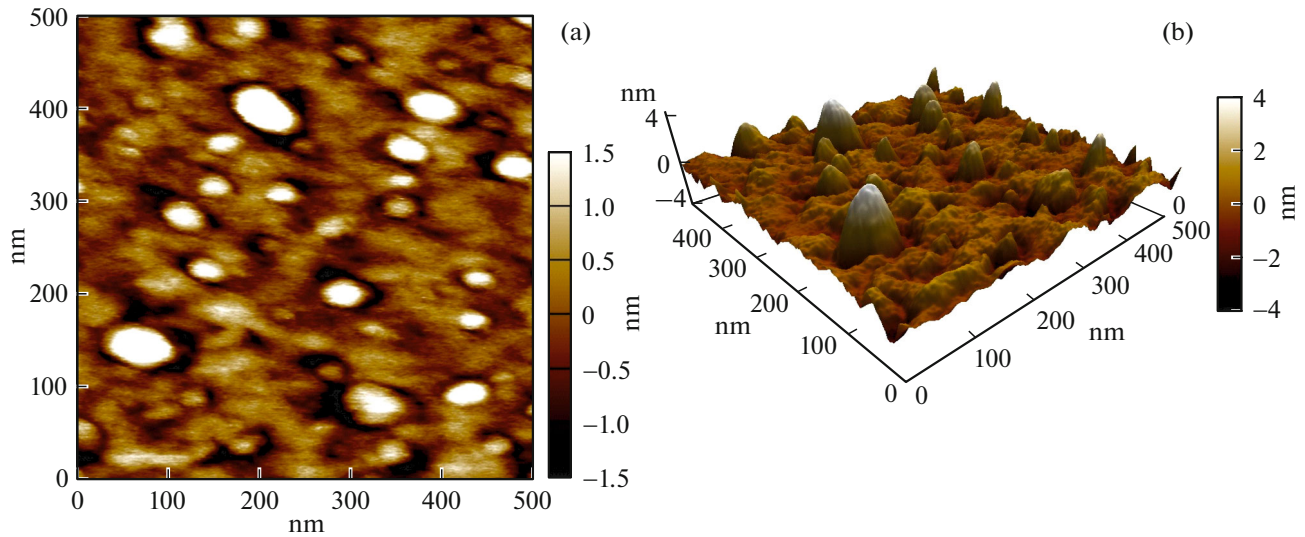
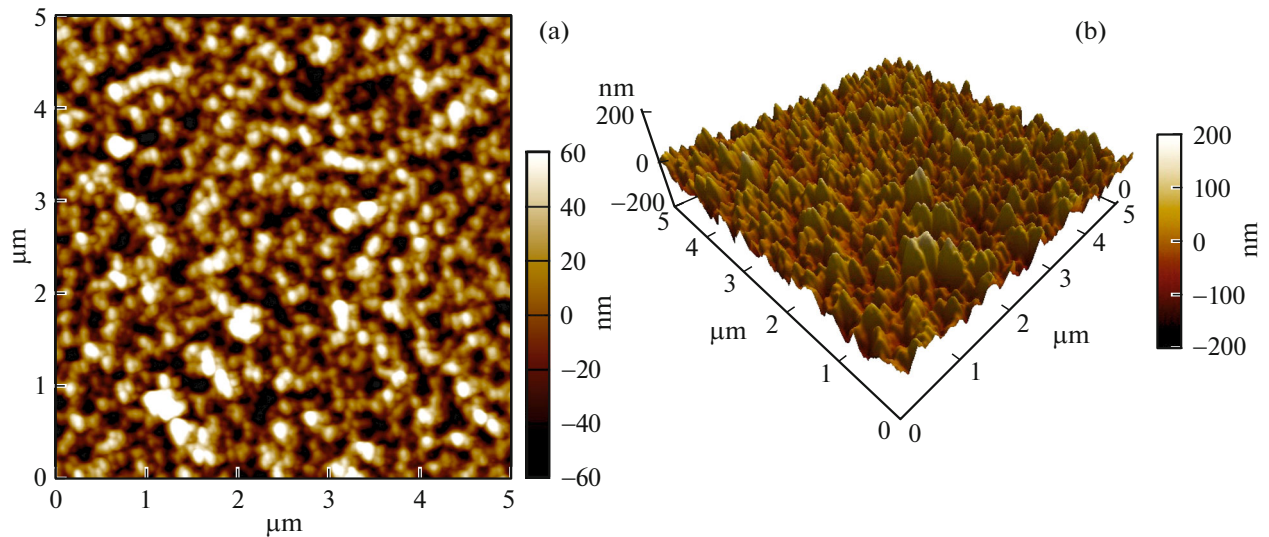**Fig. 2.** (a) 2D and (b) 3D AFM images of the Si sample surface after Zn/O implantation.


Fig. 3. (a) 2D and (b) 3D AFM images of the Si sample surface after photonic annealing at an effective temperature of 700°C.

a natural silicon-oxide surface layer of such thickness. It should be noted that both samples (curves *1* and *2*) have a surface layer with a thickness from 5−10 nm with a high content of contamination by hydrocarbon compounds.

The distribution profile of the Zn^+ concentration over the sample depth after annealing at an effective temperature of 700°C is shown in Fig. 4 (curve *4*). Calibration of this profile over the concentration was performed with respect to the coefficient of the relative elemental sensitivity calculated due to calibration of the Zn concentration profile shown in Fig. 4 (curve *2*). The maximal concentration after annealing shifted to a depth of 65 nm and corresponds to a concentration

of 2.5×10^{21} cm^{-3}. The recalculated dose of incorporated Zn in this sample is 1.5×10^{16} cm^{-2}, i.e., it decreased threefold when compared with the implantation dose. The Zn distribution after annealing, in addition to the main maximum discussed above, also has an additional surface maximum with a value of 4×10^{22} cm^{-3}, which is an order of magnitude smaller when compared with the main maximum. Such a decrease in the surface maximum of Zn is associated with the removal of hydrocarbon compounds upon annealing.

Figure 5 shows the profiles over the sample depth for currents of main negative oxide ions with substrate sputtering by Cs^+ ions with an energy of 0.5 keV. These
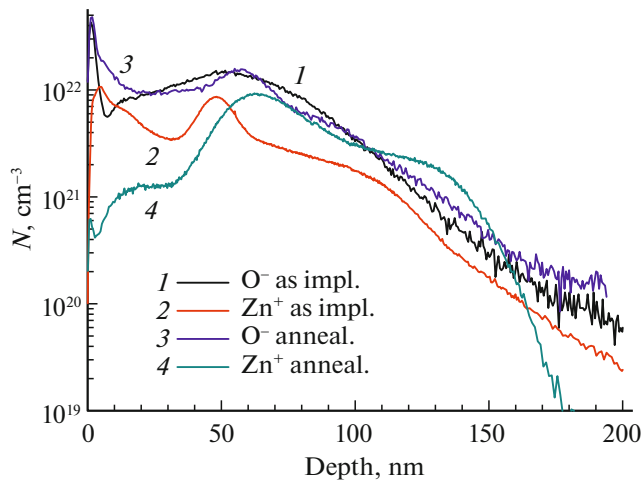
Fig. 4. Distribution profiles of O and Zn over depth in the samples under study: ions O^- (*1*) and Zn^+ (*2*) after implantation; ions O^- (*3*) and Zn^+ (*4*) after annealing the samples at an effective temperature of 700°C.
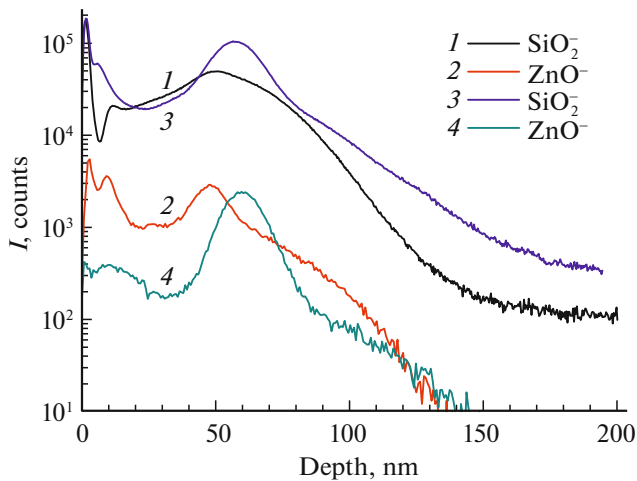
Fig. 5. Currents of the main negative oxide ions for the samples Zn/O implanted and annealed at an effective temperature of 700°C: ions SiO_2^- (*1*) and ZnO^- (*2*) for the implanted samples and SiO_2^- (*3*) and ZnO^- (*4*) for the annealed samples.

profiles qualitatively correspond to the concentration profiles both for SiO_2^- ions (curve *1*) and ZnO^- ions (curve *2*) for the samples after Zn/O implantation and for SiO_2^- ions (curve *3*) and ZnO^- ions (curve *4*) for the samples after pulsed photonic annealing at an effective temperature of 700°C, respectively. The ZnO profile after Zn/O implantation has the main maximum at a depth of 50 nm, which corresponds to the main Zn maximum after implantation. The distribution profile of the Zn-implanted ZnO^- current has, in addition to the main maximum, an additional surface maximum in the form of a doublet at a depth of 5−15 nm larger

by a factor of 2−3 than the main maximum. It was already noted above that this can be associated both with the segregation of ZnO due to the presence of the silicon-oxide surface layer and due to the presence of surface hydrocarbon contamination.

As for the current profile of SiO_2^- ions after Zn/O implantation, its maximum (Fig. 5, curve *1*) is at a depth of 55 nm, which corresponds to the maximum of implanted oxygen. It is evident that the distribution of SiO_2^- ions also has, in addition to the main maximum, a surface maximum at a depth of ~5 nm, which is caused by the presence of a natural silicon-oxide surface layer.

Both profiles considered above change after pulsed photonic annealing at an effective temperature of 700°C. Their main maxima shift into the sample to a depth of 60 nm. The main ZnO^- distribution maximum remains almost invariable in terms of magnitude, while its near-surface maximum becomes purely of the surface type and decreases by an order of magnitude.

The SiO_2 profile after photonic annealing has the following features: its main maximum increases, while the near-surface maximum does not vary either in terms of magnitude or position. This is evident because the film of the natural silicon-oxide surface layer remains in the same place.

3.3. Transmission Electron Microscopy

Figure 6 shows survey TEM images of the surface layer of the transverse sample section after Zn/O implantation for two magnifications. The distribution of implanted Zn during cold implantation with an incorporation energy of 50 keV has the maximal concentration at a depth of the predicted range $R_p = 38.4$ nm, while the distribution of implanted O at an incorporation energy of 20 keV has the maximal concentration at a depth of the predicted range $R_p = 40.0$ nm according to calculation using the SRIM program [16]. The electron diffraction pattern over the entire frame is shown in the inset to Fig. 6a. The Zn implantation region in Fig. 6a is clearly seen in the middle of the TEM image, where Zn-containing clusters and radiation-induced defects can be revealed from a variation in the image contrast. We can conclude from the analysis of reflections in the electron-diffraction pattern in the inset to Fig. 6a that twins formed in the Si substrate after implantation. The reflections from the twins are shifted by one third fraction relative to the main reflections and, as is expected, have a lower brightness. The transverse section of the reciprocal lattice is slightly reflected out of the zone axis.

Rounded spots, which comprise Zn-containing clusters, are seen in Fig. 6a in the survey TEM image with a large magnification. The amorphous state of

(a) (b)

5 nm⁻¹   100 nm   50 nm
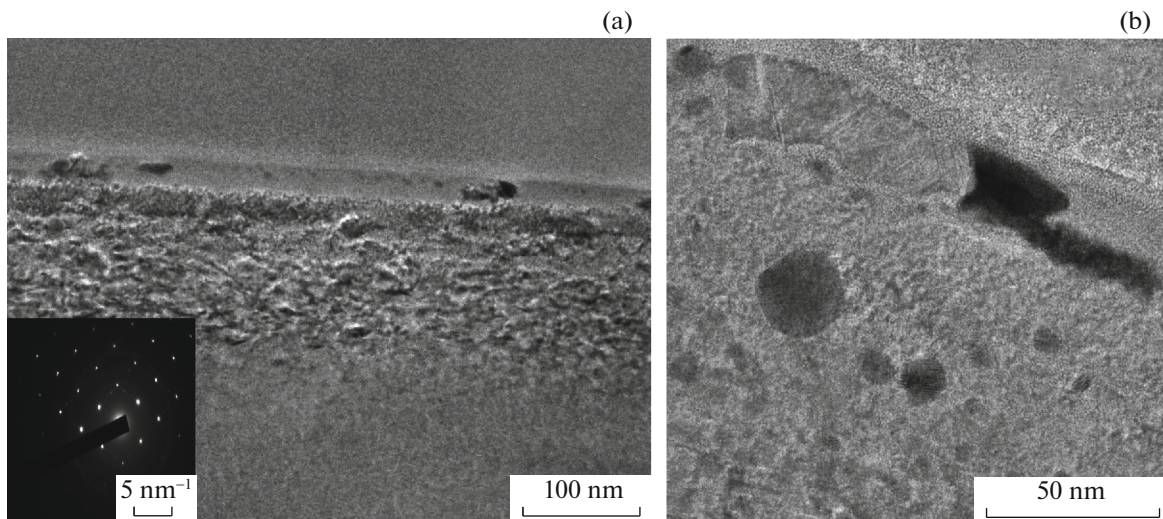
Fig. 6. Survey TEM images of the transverse section of the surface sample layer after Zn/O implantation with different degrees of magnification (a) and (b). The electron-diffraction pattern is shown in the inset.

(a) (b)

5 nm⁻¹   10 nm   10 nm
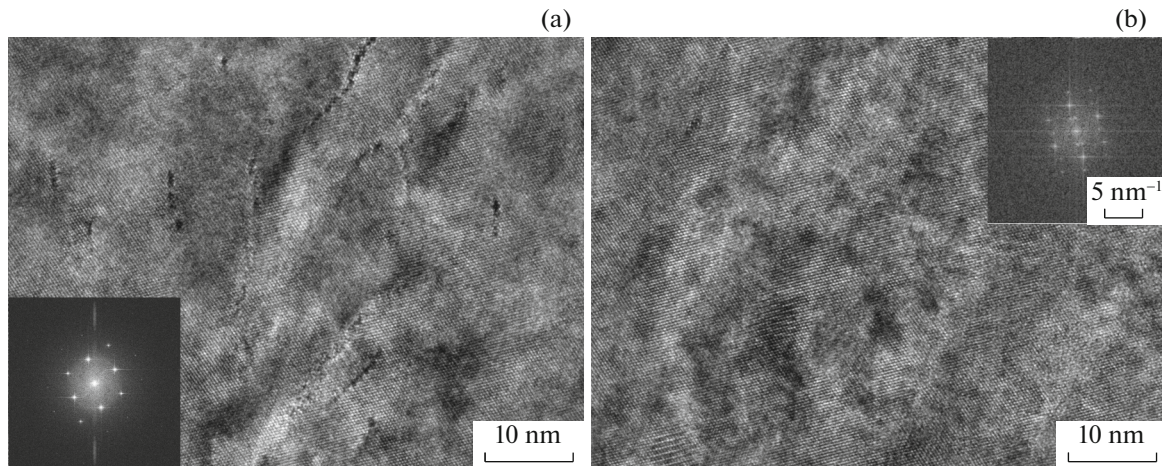
Fig. 7. HRTEM images of the transverse section of the sample surface layer after Zn/O implantation with different degrees of magnification: (a) image with dislocations, the Fourier image over the frame is shown in the inset, and (b) image with moiré spots, the Fourier image over the frame is shown in the inset.

these clusters is confirmed by the Fourier image over the entire frame (see inset in Fig. 6a), in which the traces of crystallographic planes are absent. A halo is present in this Fourier image, which evidences the partially amorphous state of the Si substrate after Zn/O implantation.

Figure 7 shows two different HRTEM images in the middle of the implantation zone for the sample after Zn/O implantation. Figure 7a shows a HRTEM image, in which dislocation segments ~10 nm in size are seen. The Fourier image over the entire frame, from which it follows, that dislocations are arranged in the silicon substrate, is presented in the inset to Fig. 7a. Figure 7b shows the HRTEM image of the near-surface layer, in which moiré spots ~20 nm in

size are seen. It follows from it that the moiré spots are caused by overlapping identical layers with different orientation and/or interplanar distance in the crystalline lattice of the silicon matrix.

3.4. Photoluminescence

Figure 8 shows the photoluminescence (PL) spectra of the samples under study in the near IR region at a temperature of 10 K. The PL spectrum after Zn/O implantation (curve *1*) demonstrates the presence of characteristic dislocation luminescence (DL) in silicon. This unambiguously evidences the presence of a considerable dislocation density in silicon after its irradiation with Zn and O ions, which agrees with the
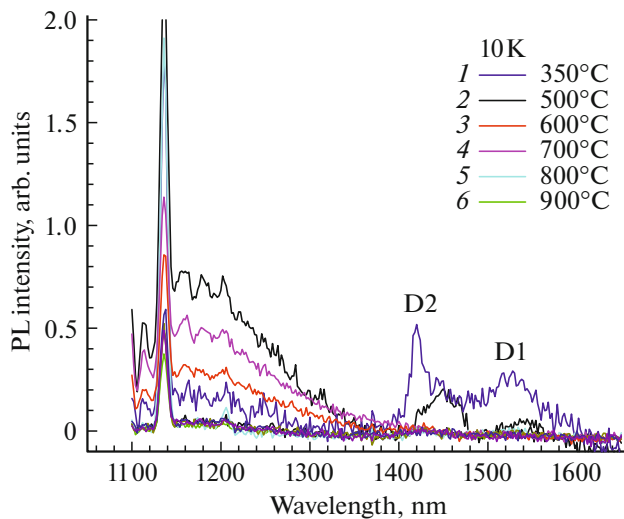
Fig. 8. PL spectra in the IR region at 10 K (curves *1* and *2* are increased threefold for clarity).

HRTEM data (Fig. 7a). It is known that the DL in silicon comprises a series of D1−D4 bands in the energy range of 0.8−1 eV [18]. It follows from the analysis of curve *1* in Fig. 8 that the short-wavelength DL part consisting of lines D4 (1.0 eV) and its phonon repetition D3 (0.934 eV) is almost absent in the PL spectrum. Since lines D3 and D4 are associated with carrier recombination at straight-linear segments of split 60-degree dislocations [19−21], the absence of these luminescence lines in the spectrum evidences the corresponding morphology of dislocations formed after the Zn/O irradiation of silicon. At the same time, the low-energy DL part consisting of lines D1 (0.81 eV) and D2 (0.87 eV), the sources of which are certain structural defects in the dislocation core, dominates in the luminescence spectrum.

Subsequent annealing of the samples at a temperature of 500°C leads to complete disappearance of the DL spectrum and the simultaneous appearance of a broad structureless band centered at ~1.07 eV, which is retained up to annealing at 700°C. The nature of these radiative centers is currently unknown. Presumably, defects in the silicon bulk, which are formed during annealing from radiation-induced defects, are responsible for them. The forming radiative centers are competitive recombination channels with respect to dislocations, which is one cause of DL quenching. In addition, dislocations formed at the lower-temperature implantation stage can be annihilated at higher temperatures, which also leads to DL quenching. Further annealing of the samples at temperatures of 800°C and higher leads to disappearance of the luminescence band centered at 1.0 eV and a considerable increase in the exciton luminescence intensity, which evidences a substantial decrease in the number of recombination centers in the silicon bulk because of their annealing.

4. CONCLUSIONS

We can conclude the following from our results.

(i) CZ *n*-type Si substrates with the orientation (100) were implanted at a temperature of 350°C by $^{64}Zn^+$ ions with a dose of 5×10^{16} cm^{-2} and energy of 50 keV and then by $^{16}O^+$ ions with a dose of 10^{17} cm^{-2} and energy of 20 keV.

(ii) Radiation-induced defects such as point defects and their clusters, twin grains, dislocations, and Zn-containing clusters (predominantly containing Zn and ZnO) with average sizes of 10−20 nm and average sizes of 20−50 nm on the Si substrate surface are formed after Zn/O implantation in the surface layer.

(iii) The gradual annealing of radiation-induced defects occurs during annealing, and Zn-containing clusters (mainly containing ZnO) of ~100 nm in size are revealed after annealing at an effective temperature of 700°C in the surface layer and on the surface of the Si substrate.

CONFLICT OF INTEREST

The authors declare that they have no conflict of interest.

REFERENCES

1. *Nanoclusters and Nanocrystals*, Ed. by H. Singh Nalwa (Hitachi, Japan, 2003).

2. C. Flytzanis, F. Haqche, M. C. Klein, D. Ricard, and Ph. Roussignol, in *Progress in Optics*, Ed. by E. Wolf (North Holland, Amsterdam, 1999), pp. 29, 321.

3. S. Chu, M. Olmedo, Zh. Yang, J. Kong, J. Liu, et al., Appl. Phys. Lett. **93**, 181106 (2008).

4. C. Y. Jiang, X. W. Sun, G. Q. Lo, D. L. Kwong, and J. X. Wang, Appl. Phys. Lett. **90**, 263501 (2007).

5. G. P. Smestad and M. Gratzel, J. Chem. Educ. **75**, 752 (1998).

6. C. Li, Y. Yang, X. W. Sun, W. Lei, X. B. Zhang, B. P. Wang, J. X. Wang, B. K. Tay, J. D. Ye, G. Q. Lo, and D. L. Kwong, Nanotechnology **18**, 135604 (2007).

7. B. B. Straumal, A. A. Mazilkin, S. G. Protasova, A. A. Myatiev, P. B. Straumal, G. Schütz, P. A. van Aken,

E. Goering, and B. Baretzky, Phys. Rev. B **79**, 205206 (2009).

8. J. S. Dodds, F. N. Meyers, and K. J. Loh, Smart Struct. Syst. **12**, 055 (2013).

9. A. Sirelkhatim, S. Mahmud, A. Seeni, N. H. M. Kaus, L. C. Ann, S. K. Mohd Bakhori, H. Hasan, and D. Mohamad, Nano-Micro Lett. **7**, 219 (2015).

10. S. Inbasekaran, R. Senthil, G. Ramamurthy, and T. P. Sastry, Int. J. Innov. Res. Sci. Eng. Technol. **3**, 8601 (2014).

11. H. Amekura, Y. Takeda, and N. Kishimoto, Mater. Lett. **222**, 96 (2011).

12. Y. Y. Shen, X. D. Zhang, D. C. Zhang, Y. H. Xue, L. H. Zhang, and C. L. Liu, Mater. Lett. **65**, 2966 (2011).

13. V. Privezentsev, V. Kulikauskas, E. Steinman, and A. Bazhenov, Phys. Status Solidi C **10**, 48 (2013).

14. V. V. Privezentsev, V. S. Kulikauskas, V. V. Zatekin, D. V. Petrov, A. Yu. Trifonov, and A. A. Batrakov,

J. Surf. Invest.: X-Ray, Synchrotr. Neutron Tech. **9**, 486 (2015).

15. J. F. Ziegler and J. P. Biersack, SRIM 2013. http://www.srim.org.

16. G. Ledoux, J. Gong, F. Huisken, O. Guillois, and C. Reynaud, Appl. Phys. Lett. **80**, 4834 (2002).

17. N. A. Drozdov, A. A. Patrin, and V. D. Tkachev, JETP Lett. **23**, 597 (1976).

18. E. A. Steinman, V. I. Vdovin, T. G. Yugova, V. S. Avrutin, and N. F. Izyumskaya, Semicond. Sci. Technol. **14**, 582 (1999).

19. R. Sauer, Ch. Kisielowski-Kemmerich, and H. Alexander, Phys. Rev. Lett. **57**, 1472 (1986).

20. A. N. Izotov, A. I. Kolyubakin, S. A. Shevchenko, and E. A. Steinman, Phys. Status Solidi A **130**, 193 (1992).

Translated by N. Korovin